A broadband tapered nanocavity for efficient nonclassical light emission

Gregersen, Niels; McCutcheon, Dara; Mørk, Jesper; Gérard, Jean-Michel; Claudon, Julien

Published in:
Optics Express

Link to article, DOI:
10.1364/OE.24.020904

Publication date:
2016

Document Version
Publisher's PDF, also known as Version of record

Research Article | Vol. 24, No. 18 | 5 Sep 2016 | OPTICS EXPRESS 20904

Optics EXPRESS

A broadband tapered nanocavity for efficient nonclassical light emission

NIELS GREGERSEN,[1,*] DARA P. S. MCCUTCHEON,[1] JESPER MØRK,[1] JEAN-MICHEL GÉRARD,[2,3] AND JULIEN CLAUDON[2,3]

[1]*DTU Fotonik, Department of Photonics Engineering, Technical University of Denmark, Ørsteds Plads Building 343, DK-2800 Kongens Lyngby, Denmark*
[2]*Univ. Grenoble Alpes, INAC-PHELIQS, F-38000 Grenoble, France*
[3]*CEA, INAC-PHELIQS, "Nanophysique et semiconducteurs" group, F-38000 Grenoble, France*
[*]*ngre@fotonik.dtu.dk*

Abstract: We present the design of a tapered nanocavity, obtained by sandwiching a photonic wire section between a planar gold reflector and a few-period Bragg mirror integrated into the tapered wire. Thanks to its ultrasmall mode volume (0.71 λ^3/n^3), this hybrid nanocavity largely enhances the spontaneous emission rate of an embedded quantum dot (Purcell factor: 6), while offering a wide operation bandwidth (full-width half-maximum: 20 nm). In addition, the top tapered section shapes the cavity far-field emission into a very directive output beam, with a Gaussian spatial profile. For realistic taper dimensions, a total outcoupling efficiency to a Gaussian beam of 0.8 is predicted. Envisioned applications include bright sources of non-classical states of light, such as widely tunable sources of indistinguishable single photons and polarization-entangled photon pairs.

OCIS codes: (140.3300) Laser beam shaping; (140.3948) Microcavity devices; (250.5590) Quantum-well, -wire and -dot devices; (350.4238) Nanophotonics and photonic crystals.

References and links

1. S. Barz, "Quantum computing with photons: introduction to the circuit model, the oneway quantum computer, and the fundamental principles of photonic experiments," J. Phys. At. Mol. Opt. Phys. **48**(8), 083001 (2015).
2. P. Lodahl, S. Mahmoodian, and S. Stobbe, "Interfacing single photons and single quantum dots with photonic nanostructures," Rev. Mod. Phys. **87**(2), 347–400 (2015).
3. A. J. Shields, "Semiconductor quantum light sources," Nat. Photonics **1**(4), 215–223 (2007).
4. T. M. Babinec, B. J. M. Hausmann, M. Khan, Y. Zhang, J. R. Maze, P. R. Hemmer, and M. Lončar, "A diamond nanowire single-photon source," Nat. Nanotechnol. **5**(3), 195–199 (2010).
5. P. Siyushev, G. Stein, J. Wrachtrup, and I. Gerhardt, "Molecular photons interfaced with alkali atoms," Nature **509**(7498), 66–70 (2014).
6. W. L. Barnes, G. Björk, J. M. Gérard, P. Jonsson, J. A. E. Wasey, P. T. Worthing, and V. Zwiller, "Solid-state single photon sources: light collection strategies," Eur. Phys. J. D **18**(2), 197–210 (2002).
7. N. Gregersen, P. Kaer, and J. Mørk, "Modeling and design of high-efficiency single-photon sources," IEEE J. Sel. Top. Quantum Electron. **19**(5), 9000516 (2013).
8. C. Santori, D. Fattal, J. Vucković, G. S. Solomon, and Y. Yamamoto, "Indistinguishable photons from a single-photon device," Nature **419**(6907), 594–597 (2002).
9. A. Berthelot, I. Favero, G. Cassabois, C. Voisin, C. Delalande, Ph. Roussignol, R. Ferreira, and J. M. Gérard, "Unconventional motional narrowing in the optical spectrum of a semiconductor quantum dot," Nat. Phys. **2**(11), 759–764 (2006).
10. A. Thoma, P. Schnauber, M. Gschrey, M. Seifried, J. Wolters, J.-H. Schulze, A. Strittmatter, S. Rodt, A. Carmele, A. Knorr, T. Heindel, and S. Reitzenstein, "Exploring dephasing of a solid-state quantum emitter via time- and temperature-dependent Hong-Ou-mandel experiments," Phys. Rev. Lett. **116**(3), 033601 (2016).
11. P. Kaer, N. Gregersen, and J. Mørk, "The role of phonon scattering in the indistinguishability of photons emitted from semiconductor cavity QED systems," New J. Phys. **15**(3), 035027 (2013).
12. S. Unsleber, D. P. S. McCutcheon, M. Dambach, M. Lermer, N. Gregersen, S. Höfling, J. Mørk, C. Schneider, and M. Kamp, "Two-photon interference from a quantum dot microcavity: Persistent pure dephasing and suppression of time jitter," Phys. Rev. B **91**(7), 075413 (2015).
13. P. Kaer and J. Mørk, "Decoherence in semiconductor cavity QED systems due to phonon couplings," Phys. Rev. B **90**(3), 035312 (2014).

#264431 http://dx.doi.org/10.1364/OE.24.020904
Journal © 2016 Received 2 May 2016; revised 25 Jun 2016; accepted 27 Jun 2016; published 31 Aug 2016

Optics EXPRESS

14. J. Claudon, J. Bleuse, N. S. Malik, M. Bazin, P. Jaffrennou, N. Gregersen, C. Sauvan, P. Lalanne, and J. M. Gérard, "A highly efficient single-photon source based on a quantum dot in a photonic nanowire," Nat. Photonics **4**, 174–177 (2010).
15. M. Munsch, N. S. Malik, E. Dupuy, A. Delga, J. Bleuse, J. M. Gérard, J. Claudon, N. Gregersen, and J. Mørk, "Dielectric GaAs antenna ensuring an efficient broadband coupling between an InAs quantum dot and a Gaussian optical beam," Phys. Rev. Lett. **110**(17), 177402 (2013).
16. Y.-M. He, Y. He, Y.-J. Wei, D. Wu, M. Atatüre, C. Schneider, S. Höfling, M. Kamp, C.-Y. Lu, and J.-W. Pan, "On-demand semiconductor single-photon source with near-unity indistinguishability," Nat. Nanotechnol. **8**(3), 213–217 (2013).
17. Y.-J. Wei, Y.-M. He, M.-C. Chen, Y.-N. Hu, Y. He, D. Wu, C. Schneider, M. Kamp, S. Höfling, C.-Y. Lu, and J.-W. Pan, "Deterministic and robust generation of single photons from a single quantum dot with 99.5% indistinguishability using adiabatic rapid passage," Nano Lett. **14**(11), 6515–6519 (2014).
18. K. J. Vahala, "Optical microcavities," Nature **424**(6950), 839–846 (2003).
19. J. M. Gérard, "Solid-state cavity-quantum electrodynamics with self-assembled quantum dots," in *Single Quantum Dots*, Top. Appl. Phys. 90, P. Michler, ed. (Springer, 2003), pp. 269–315.
20. J. M. Gérard and B. Gayral, "Strong purcell effect for InAs quantum boxes in three-dimensional solid-state microcavities," J. Lightwave Technol. **17**(11), 2089–2095 (1999).
21. O. Gazzano, S. Michaelis de Vasconcellos, C. Arnold, A. Nowak, E. Galopin, I. Sagnes, L. Lanco, A. Lemaître, and P. Senellart, "Bright solid-state sources of indistinguishable single photons," Nat. Commun. **4**, 1425 (2013).
22. A. Dousse, L. Lanco, J. Suffczyński, E. Semenova, A. Miard, A. Lemaître, I. Sagnes, C. Roblin, J. Bloch, and P. Senellart, "Controlled light-matter coupling for a single quantum dot embedded in a pillar microcavity using far-field optical lithography," Phys. Rev. Lett. **101**(26), 267404 (2008).
23. X. Ding, Y. He, Z.-C. Duan, N. Gregersen, M.-C. Chen, S. Unsleber, S. Maier, C. Schneider, M. Kamp, S. Höfling, C.-Y. Lu, and J.-W. Pan, "On-demand single photons with high extraction efficiency and near-unity indistinguishability from a resonantly driven quantum dot in a micropillar," Phys. Rev. Lett. **116**(2), 020401 (2016).
24. N. Somaschi, V. Giesz, L. De Santis, J. C. Loredo, M. P. Almeida, G. Hornecker, S. L. Portalupi, T. Grange, C. Antón, J. Demory, C. Gómez, I. Sagnes, N. D. Lanzillotti-Kimura, A. Lemaítre, A. Auffeves, A. G. White, L. Lanco, and P. Senellart, "Near-optimal single-photon sources in the solid state," Nat. Photonics **10**(5), 340–345 (2016).
25. A. Dousse, J. Suffczyński, A. Beveratos, O. Krebs, A. Lemaître, I. Sagnes, J. Bloch, P. Voisin, and P. Senellart, "Ultrabright source of entangled photon pairs," Nature **466**(7303), 217–220 (2010).
26. M. Gschrey, A. Thoma, P. Schnauber, M. Seifried, R. Schmidt, B. Wohlfeil, L. Krüger, J.-H. Schulze, T. Heindel, S. Burger, F. Schmidt, A. Strittmatter, S. Rodt, and S. Reitzenstein, "Highly indistinguishable photons from deterministic quantum-dot microlenses utilizing three-dimensional in situ electron-beam lithography," Nat. Commun. **6**, 7662 (2015).
27. M. E. Reimer, G. Bulgarini, N. Akopian, M. Hocevar, M. B. Bavinck, M. A. Verheijen, E. P. A. M. Bakkers, L. P. Kouwenhoven, and V. Zwiller, "Bright single-photon sources in bottom-up tailored nanowires," Nat. Commun. **3**, 737 (2012).
28. G. Bulgarini, M. E. Reimer, M. Bouwes Bavinck, K. D. Jöns, D. Dalacu, P. J. Poole, E. P. A. M. Bakkers, and V. Zwiller, "Nanowire waveguides launching single photons in a Gaussian mode for ideal fiber coupling," Nano Lett. **14**(7), 4102–4106 (2014).
29. P. E. Kremer, A. C. Dada, P. Kumar, Y. Ma, S. Kumar, E. Clarke, and B. D. Gerardot, "Strain-tunable quantum dot embedded in a nanowire antenna," Phys. Rev. B **90**(20), 201408 (2014).
30. J. Claudon, N. Gregersen, P. Lalanne, and J. M. Gérard, "Harnessing light with photonic nanowires: fundamentals and applications to quantum optics," ChemPhysChem **14**(11), 2393–2402 (2013).
31. J. Bleuse, J. Claudon, M. Creasey, N. S. Malik, J. M. Gérard, I. Maksymov, J. P. Hugonin, and P. Lalanne, "Inhibition, enhancement, and control of spontaneous emission in photonic nanowires," Phys. Rev. Lett. **106**(10), 103601 (2011).
32. Y.-R. Nowicki-Bringuier, R. Hahner, J. Claudon, G. Lecamp, P. Lalanne, and J. M. Gérard, "A novel high-efficiency single-mode single photon source," Ann. Phys. **32**(2-3), 151–154 (2008).
33. I. Friedler, C. Sauvan, J. P. Hugonin, P. Lalanne, J. Claudon, and J. M. Gérard, "Solid-state single photon sources: the nanowire antenna," Opt. Express **17**(4), 2095–2110 (2009).
34. N. Gregersen, T. R. Nielsen, J. Mørk, J. Claudon, and J. M. Gérard, "Designs for high-efficiency electrically pumped photonic nanowire single-photon sources," Opt. Express **18**(20), 21204–21218 (2010).
35. P. Stepanov, A. Delga, N. Gregersen, E. Peinke, M. Munsch, J. Teissier, J. Mørk, M. Richard, J. Bleuse, J. M. Gérard, and J. Claudon, "Highly directive and Gaussian far-field emission from 'giant' photonic trumpets," Appl. Phys. Lett. **107**(14), 141106 (2015).
36. D. Cadeddu, J. Teissier, F. R. Braakman, N. Gregersen, P. Stepanov, J. M. Gérard, J. Claudon, R. J. Warburton, M. Poggio, and M. Munsch, "A fiber-coupled quantum-dot on a photonic tip," Appl. Phys. Lett. **108**(1), 011112 (2016).
37. I. S. Maksymov, M. Besbes, J. P. Hugonin, J. Yang, A. Beveratos, I. Sagnes, I. Robert-Philip, and P. Lalanne, "Metal-coated nanocylinder cavity for broadband nonclassical light emission," Phys. Rev. Lett. **105**(18), 180502 (2010).

Optics EXPRESS

38. J. T. Choy, B. J. M. Hausmann, T. M. Babinec, I. Bulu, M. Khan, P. Maletinsky, A. Yacoby, and M. Lončar, "Enhanced single-photon emission from a diamond–silver aperture," Nat. Photonics **5**(12), 738–743 (2011).
39. L. Chen and E. Towe, "Nanowire lasers with distributed-Bragg-reflector mirrors," Appl. Phys. Lett. **89**(5), 053125 (2006).
40. I. Friedler, P. Lalanne, J. P. Hugonin, J. Claudon, J. M. Gérard, A. Beveratos, and I. Robert-Philip, "Efficient photonic mirrors for semiconductor nanowires," Opt. Lett. **33**(22), 2635–2637 (2008).
41. S. Gehrsitz, F. K. Reinhart, C. Gourgon, N. Herres, A. Vonlanthen, and H. Sigg, "The refractive index of $Al_xGa_{1-x}As$ below the band gap: Accurate determination and empirical modeling," J. Appl. Phys. **87**(11), 7825–7837 (2000).
42. P. B. Johnson and R. W. Christy, "Optical constants of the noble metals," Phys. Rev. B **6**(12), 4370–4379 (1972).
43. H. Malitson, "Interspecimen comparison of the refractive index of fused silica," J. Opt. Soc. Am. **55**(10), 1205–1209 (1963).
44. T. Bååk, "Silicon oxynitride; a material for GRIN optics," Appl. Opt. **21**(6), 1069–1072 (1982).
45. T. Suhr, N. Gregersen, K. Yvind, and J. Mørk, "Modulation response of nanoLEDs and nanolasers exploiting Purcell enhanced spontaneous emission," Opt. Express **18**(11), 11230–11241 (2010).
46. A. Naesby, T. Suhr, P. T. Kristensen, and J. Mørk, "Influence of pure dephasing on emission spectra from single photon sources," Phys. Rev. A **78**(4), 045802 (2008).
47. A. Auffèves, D. Gerace, J.-M. Gérard, M. F. Santos, L. C. Andreani, and J.-P. Poizat, "Controlling the dynamics of a coupled atom-cavity system by pure dephasing," Phys. Rev. B **81**(24), 245419 (2010).
48. P. Kaer, T. R. Nielsen, P. Lodahl, A.-P. Jauho, and J. Mørk, "Microscopic theory of phonon-induced effects on semiconductor quantum dot decay dynamics in cavity QED," Phys. Rev. B **86**(8), 085302 (2012).
49. Q. Mermillod, T. Jakubczyk, V. Delmonte, A. Delga, E. Peinke, J.-M. Gérard, J. Claudon, and J. Kasprzak, "Harvesting, coupling, and control of single-exciton coherences in photonic waveguide antennas," Phys. Rev. Lett. **116**(16), 163903 (2016).
50. P. Bienstman and R. Baets, "Optical modelling of photonic crystals and VCSELs using eigenmode expansion and perfectly matched layers," Opt. Quantum Electron. **33**(4/5), 327–341 (2001).
51. N. Gregersen and J. Mørk, "An improved perfectly matched layer for the eigenmode expansion technique," Opt. Quantum Electron. **40**(11-12), 957–966 (2008).
52. N. Gregersen, T. R. Nielsen, B. Tromborg, and J. Mørk, "Quality factors of nonideal micro pillars," Appl. Phys. Lett. **91**(1), 011116 (2007).
53. P. Lalanne, J. P. Hugonin, and J. M. Gérard, "Electromagnetic study of the quality factor of pillar microcavities in the small diameter limit," Appl. Phys. Lett. **84**(23), 4726–4728 (2004).
54. Y. Akahane, T. Asano, B.-S. Song, and S. Noda, "High-Q photonic nanocavity in a two-dimensional photonic crystal," Nature **425**(6961), 944–947 (2003).
55. M. Nomura, K. Tanabe, S. Iwamoto, and Y. Arakawa, "Design of a high-Q H0 photonic crystal nanocavity for cavity QED," Phys. Status Solidi **8**(2), 340–342 (2011).
56. N. Akopian, L. Wang, A. Rastelli, O. G. Schmidt, and V. Zwiller, "Hybrid semiconductor-atomic interface: slowing down single photons from a quantum dot," Nat. Photonics **5**(4), 230–233 (2011).
57. N. Akopian, U. Perinetti, L. Wang, A. Rastelli, O. G. Schmidt, and V. Zwiller, "Tuning single GaAs quantum dots in resonance with a rubidium vapor," Appl. Phys. Lett. **97**(8), 082103 (2010).
58. R. Trotta and A. Rastelli, "Engineering of quantum dot photon sources via electro-elastic fields," in *Engineering the Atom-Photon Interaction*, A. Predojević and M. W. Mitchell, eds. (2015), pp. 277–302.

1. Introduction

Within optical quantum information processing [1] and linear optics quantum computing, the quantum bits are encoded in single photons. A key component is thus a highly efficient source emitting single indistinguishable photons on-demand [2]. A well-established platform for such a deterministic single-photon source (SPS) is based on a quantum emitter, e.g. a semiconductor quantum dot (QD) [3], a nitrogen-vacancy center [4] or an organic dye molecule [5] in a host material. Though quantum efficiencies can be very high for these systems, achieving high extraction efficiency represents a major challenge in SPS engineering, and an important figure of merit is the collection efficiency ε [6] defined as the probability of collecting a photon into the first lens of the optical detection setup per emission event. In the case of a quantum emitter in a semiconductor bulk material, the majority of the emitted light is reflected at the semiconductor-air interface and the resulting collection efficiency is typically restricted to only a few percent. To achieve high efficiency, it is thus necessary to place the emitter inside a structured environment [6,7] in order to control the light emission and ensure a good coupling to the collection optics.

Another important figure of merit is the indistinguishability of emitted photons [8] measured as one minus the normalized area of the $\tau = 0$ peak in a Hong-Ou-Mandel two-

Optics EXPRESS

photon interference experiment. Whereas the coherence time in atomic systems is generally life-time limited, emitters in solid-state systems interact with the environment leading to decreased coherence times and reduced indistinguishability. Decoherence mechanisms include fast fluctuations of the exciton energy due to Coulomb interaction with the electrostatic environment of the QD [9] occurring on a few ns timescale [10] as well as phonon-induced decoherence arising as a result of interactions between excitons and lattice vibrations in the solid-state environment via deformation potential coupling [11–13]. High-efficiency SPSs generally operate in the weak QED coupling regime, where the impact of these decoherence mechanisms can be significant since the photon emission time is longer [11] than the characteristic emitter-phonon interaction or exciton energy fluctuation timescales. It is thus beneficial to accelerate the photon emission rate to overcome both phonon-induced decoherence and spectral diffusion.

While highly efficient single-photon generation [14,15] and highly indistinguishable photon emission [16,17] have each been reported separately, the development of an SPS displaying both properties simultaneously is still a major open challenge, which requires further conceptual and design efforts to be successfully addressed. Conceptually, the microcavity [18] approach relies on significant Purcell enhancement to ensure a high efficiency [19,20], and a careful spectral alignment of the cavity and the emitter lines as well as a spatial alignment of the emitter position and the field maximum are thus required. An efficiency of 0.79 was demonstrated for a micropillar SPS [21] fabricated using an in situ fabrication technique [22] to achieve both alignments. The micropillar SPS benefits from the Purcell effect to accelerate photon emission, and in the same work an indistinguishability of 0.82 was demonstrated [21] using non-resonant excitation for a micropillar with a Purcell enhancement of 3.9. To improve the indistinguishability several groups have implemented resonant fluorescence excitation to avoid time-jitter-induced decoherence, which has led to the very recent demonstrations of 0.99 indistinguishability combined with extraction efficiencies of 0.6 for micropillar SPSs fabricated using a randomly positioned QD [23] or using in situ fabrication [24]. These devices benefit from the Purcell effect to accelerate photon emission with Purcell factors of ~6-7. However, a drawback of the microcavity approach is its narrow band preventing large tuning of the QD emission line. Additionally, since entangled photon pair generation using the exciton-biexciton cascade requires efficient outcoupling of both the exciton and the biexciton transitions, rather complex dual-cavity schemes [25] are required for entangled photon pair generation.

To overcome these limitations, broadband approaches are currently actively investigated. Among the ones which offer a far-field emission perpendicular to the chip plane, the microlens SPS defined by in situ fabrication has recently demonstrated an indistinguishability of 0.80 and an efficiency of 0.23 [26]. Another appealing approach is based on a QD inserted in a photonic nanowire (PW) antenna [14,15,27–36]. A broadband geometrical field-screening effect [30–32] suppresses spontaneous emission into radiation modes and ensures preferential coupling from the QD to the fundamental waveguide mode. There is no resonant Purcell effect and no cavity-emitter spectral alignment is required, which represents a major simplification in the fabrication. Using an integrated bottom mirror and a tapered tip to engineer the radiation pattern [33], high efficiency PW-SPSs have been demonstrated. An efficiency of 0.72 has been demonstrated for “needle”-like PWs taking benefit of a regular conical tapering of the output end [14]. A second generation of devices is based on the PW “trumpet” design with an inverted conical taper [34]. It has demonstrated an efficiency of 0.75 [15] and delivers an output beam with a Gaussian angular profile [35]. In addition, this approach is compatible with electrical contacting, and extension of the top nanowire diameter allows for either highly directive, Gaussian far-field emission or direct “butt” coupling to an optical fiber [35,36]. However, the absence of significant Purcell enhancement leads to slow spontaneous emission, potentially vulnerable to phonon-induced decoherence and spectral diffusion.

Optics EXPRESS

In this work, we extend the photonic trumpet design by implementing a weak cavity QED effect with the purpose of increasing the spontaneous emission rate via the Purcell effect. This is achieved by implementing a distributed Bragg reflector (DBR) in the inverted conical taper. The resonant cavity QED effect introduced in this work is identical to that used for the micropillar SPS, however since the Purcell factor is proportional to Q/V and since the nanowire area is two orders of magnitude smaller than that of a typical micropillar, significant Purcell enhancement can be obtained for modest Q factors. Indeed, we will show that a Purcell factor of 6 for a remarkable 20 nm full-width half-maximum (FWHM) of the resonance is achievable combined with an efficiency of 0.8. So far, broadband Purcell enhancement from SPSs, typically exploiting plasmonic effects to decrease the mode volume, has been proposed previously [37,38], however at the cost of significantly reduced efficiency compared to our trumpet PW design approach. The combination of large Purcell enhancement and large efficiency, maintained over a broad operation bandwidth offer appealing perspectives to realize advanced quantum light sources. An accelerated photon emission rate lowers the relative influence of decoherence due to phonon interaction and spectral diffusion and is therefore expected to significantly improve the indistinguishability of the emitted photons. The proposed structure could thus find a first application to the realization of bright and largely tunable sources of indistinguishable single photons. In addition, this photonic structure is well suited to realize a bright source of polarization-entangled photon pairs which exploits the QD exciton-biexciton cascade. Indeed, the broad operation bandwidth naturally ensures an efficient collection of exciton and biexcition photons, while the Purcell effect alleviates the stringent requirements on the excitonic fine structure splitting [25].

The implementation of DBRs in PWs was initially suggested [39] for the PW laser as a means to reduce mirror loss and decrease the lasing threshold. Shortly after, the AlGaAs DBR was considered for the PW-SPS application [40]. In the latter work, it was shown that, for a wavelength λ and a PW refractive index n, the reflectivity of the PW-DBR is significantly reduced for PW diameters below $\sim\lambda/n$ due to poor modal overlap of the fundamental mode in the GaAs/AlAs layers. While the overlap can be improved by reducing the index contrasts, this occurs at the expense of a reduction of the DBR reflectivity per layer leading to an unrealistic number of layer pairs required for near-unity reflectivity as well as significantly reduced bandwidth. For this reason, the DBR was not used as bottom mirror in the initial high-efficiency PW-SPSs [14,15], which instead adopted a gold-silica mirror strategy [33,34,40]. Whereas the DBR is unsuitable as bottom mirror, the PW trumpet design allows for the implementation of a DBR as a top mirror in the inverted conical taper. This is achieved simply by placing the DBR in a taper region with sufficiently large diameter to ensure a good fundamental modal overlap. The ability of employing a DBR in the trumpet PW-SPS represents a unique asset of this design, which is fully exploited in this work.

This article is organized as follows. In Section 2, the photonic trumpet geometry with DBR is introduced. Section 3 presents our single-mode model based on an element-splitting approach to describe the Purcell factor and the efficiency. In Section 4, the new elements of the SPS geometry are analyzed. The performance of the full design is studied in Section 5 and is discussed in Section 6. We conclude our work in Section 7. Finally, the Appendix provides additional element analyses as well as a detailed growth recipe for the structure.

2. Photonic trumpet geometry

The photonic nanowire is a vertical rotationally symmetric GaAs cylinder placed on a substrate [30]. The design is illustrated in Fig. 1. Single photons are emitted by an InAs QD assumed to be positioned on the axis of the nanowire. The QD is modeled as a point source with in-plane dipole moment, where the small perturbation due to the slightly modified refractive index profile of the QD is ignored. For an optimum nanowire radius, 96% of the emitted photons are coupled to the fundamental waveguide mode. The design is then conceptually divided into two sections. To control the light emission and ensure a good

Optics EXPRESS

coupling to the lens, the fundamental mode must undergo an adiabatic expansion to reduce the divergence of the output beam. This takes place in the top Section I, where we adopt the photonic trumpet design approach [34] featuring an inverted conical taper and a top silicon-nitride anti-reflection coating. Half of the emitted photons propagate towards the substrate, and the gold-silica mirror [40] in the bottom Section II is incorporated to reflect this light back towards the top. Such a mirror, which displays far superior properties compared to either a planar DBR, a bare metallic mirror or a DBR integrated in the PW, provides a 0.91 modal reflectivity for the fundamental HE_{11} guided mode. The bare trumpet design features no top mirror and gives rise to a relative spontaneous emission enhancement of only 1.8 due to the presence of the bottom metal mirror.

Table 1. Material refractive indices.

Material	Refractive index	Reference
GaAs	3.48 @ 925 nm [a]	[41]
$Al_{0.85}Ga_{0.15}As$	2.99 @ 925 nm [a]	[41]
Au	0.18 + 5.9i	[42]
SiO_2	1.45	[43]
Si_3N_4	1.99	[44]

[a] A wavelength-dependent refractive index model [41] is used.

The aim of this work is to propose a design implementing a GaAs/AlGaAs DBR in the inverted conical taper allowing for the realization of a cavity QED effect in the weak coupling regime. Significant Purcell enhancement can be obtained by placing a DBR inside the original trumpet geometry design. However, this cavity QED effect introduces two trade-offs. For a bottom mirror with reflection coefficient of less than unity, the introduction of the top DBR will reduce the efficiency. There will thus be a trade-off between Purcell enhancement and efficiency. Additionally, the broadband performance of the original photonic nanowire design will be compromised due to the resonant cavity QED effect. Thus, the Purcell factor, the linewidth and the efficiency should be studied simultaneously to identify a suitable design.

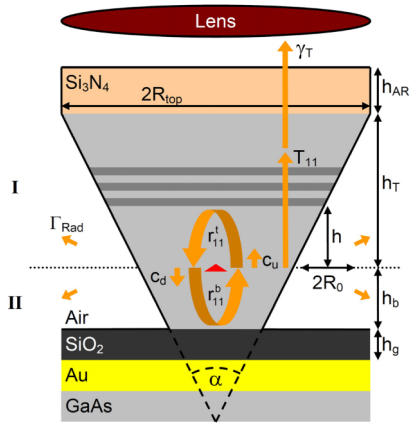

Fig. 1. The photonic trumpet SPS design featuring a DBR in the inverted taper. The structure is divided into a top taper element in Section I and a bottom metal mirror in Section II separated by the dotted line at the QD layer, where the QD is represented by the red triangle.

The design wavelength is chosen to be λ = 925 nm, which is typical for InAs/GaAs QDs used in quantum optics experiments and devices, and the material parameters are listed in Table 1 for a temperature of 10° K. A reduced 85% Al concentration was chosen in the AlGaAs layer to avoid potential oxidation of pure AlAs from the PW sidewalls. The exact growth recipe for the DBR is provided in Appendix C.

Optics EXPRESS

3. The elements-splitting approach

The SPS efficiency can be computed by placing a dipole emitter inside the full structure, computing the field and evaluating the far-field emission pattern of the full structure. Though rigorous, this procedure does not give direct insight into the governing physics. For this reason we employ a single-mode model based on a well-established element-splitting approach [33,34]. This approach allows us to separately analyze and optimize the various elements of the SPS design. The main assumption of the model is that the spontaneous emission rate into radiation modes Γ_{Rad} for the full structure is identical to that of the infinite nanowire. The validity of this assumption has been confirmed by comparison with full calculations in previous works [33,34].

3.1 Model

We now consider the propagation of the fundamental HE_{11} waveguide mode in the full structure illustrated in Fig. 1. The spontaneous emission rate from the QD into the HE_{11} mode of an infinitely long uniform nanowire is Γ_{HE11}, and the amplitude coefficients of the upwards and downwards propagating fundamental mode at the position of the QD layer are denoted c_u and c_d. The coefficients r_{11}^t and r_{11}^b are the complex modal HE_{11} reflection coefficients for the top and bottom reflectors respectively as seen from the QD layer, such that the phase term due to mode propagation from the QD layer to the DBR (metal mirror) and back is included in r_{11}^t (r_{11}^b). Finally, T_{11} and γ_{T} are the power HE_{11} transmission coefficients from the QD layer through the DBR and from the top of the DBR to the lens, respectively.

The efficiency ε is evaluated as

$$\varepsilon = \frac{\gamma |c_u|^2}{\Gamma_{\mathrm{T}}}, \tag{1}$$

where $\gamma \equiv T_{11}\gamma_{\mathrm{T}}$ is the total power transmission from the QD to the lens and Γ_{T} is the total spontaneous emission rate. For a QD in an infinitely long nanowire, the amplitude coefficients are given by $c_u = c_d = c_0 \equiv \mathrm{sqrt}(\Gamma_{\mathrm{HE11}}/2)$. In the presence of the DBR and the metal mirror, the coefficients are given by

$$c_u = c_0 \frac{1 + r_{11}^b}{1 - r_{11}^t r_{11}^b} \tag{2}$$

$$c_d = c_0 \frac{1 + r_{11}^t}{1 - r_{11}^t r_{11}^b}, \tag{3}$$

and the corresponding total spontaneous emission rate Γ_{T} is computed as

$$\Gamma_{\mathrm{T}} = \left(1 - \left|r_{11}^t\right|^2\right)|c_u|^2 + \left(1 - \left|r_{11}^b\right|^2\right)|c_d|^2 + \Gamma_{\mathrm{Rad}}. \tag{4}$$

As for the efficiency, we would like to describe the spontaneous emission rate Γ_{M} into the cavity mode as an explicit function of the scattering coefficients. A general expression for the rate Γ_{M} normalized to the rate Γ_0 in a bulk material is given by

$$\frac{\Gamma_{\mathrm{M}}}{\Gamma_0} = \mathrm{Re}\left[\frac{\left(1 + r_{11}^t\right)\left(1 + r_{11}^b\right)}{1 - r_{11}^t r_{11}^b}\right]\frac{\Gamma_{\mathrm{HE11}}}{\Gamma_0} \equiv F_{\mathrm{P}}^{\mathrm{G}}. \tag{5}$$

Optics EXPRESS

In its derivation no assumptions about the spatial and spectral QD-cavity alignment have been made, and Eq. (5) thus correctly describes the normalized emission rate into the HE_{11} mode at an arbitrary wavelength.

Now, the Purcell factor F_P also describes the normalized spontaneous emission rate into the cavity mode and is traditionally given as

$$F_P = \frac{\Gamma_M}{\Gamma_0} = \frac{3}{4\pi^2}\frac{Q}{V}\left(\frac{\lambda}{n}\right)^3, \tag{6}$$

where Q is the cavity quality factor and V is the mode volume. Comparing Eqs. (5) and (6) we observe that both describe the normalized spontaneous emission rate into the cavity mode. While the ratio Q/V is not explicitly present in Eq. (5), it appears implicitly via the reflection coefficients and the rate Γ_{HE11}, and the ratio Q/V thus still governs the spontaneous emission rate of our single-mode model on resonance. However, a difference between the two expressions is that Eq. (6) only holds at the cavity resonance and for an emitter located on the field maximum, whereas Eq. (5) is valid for arbitrary wavelengths and emitter positions. We can thus consider Eq. (5) as a generalization of the Purcell factor valid at all wavelengths. This generalized Purcell factor F_P^G should be understood as a local density of states at the position of the emitter well defined for all wavelengths, and our model thus correctly predicts both the efficiency and F_P^G also in the off-resonance case. In the following we skip the ^{G} superscript for simplicity and refer to the generalized Purcell factor simply as the Purcell factor. We remark that the Eqs. (5) and (6) assume that the emitter linewidth is narrow compared to the cavity linewidth. If it is not, an integration over the electronic density of states must be performed [45–47]. For our low-Q cavity, the cavity linewidth is indeed orders of magnitude larger than typical InAs QD emitter linewidths, and Eqs. (5) and (6) can be employed safely.

Finally, we compute the Q factor using

$$Q = \frac{-\lambda_r}{2\left(1-\left|r_{11}^t r_{11}^b\right|\right)}\frac{\partial}{\partial\lambda}\arg\left(r_{11}^t r_{11}^b\right), \tag{7}$$

where λ_r is the resonance wavelength such that $\arg\left(r_{11}^t r_{11}^b\right) = 0$.

The elements-splitting approach thus allows us to analyze and optimize the scalar scattering coefficients r_{11}^t, r_{11}^b, T_{11} and γ_T and the spontaneous emission rates Γ_{HE11} and Γ_{Rad} separately. We use the single-mode model of Eqs. (1)-(7) to analyze the physics, however the scattering coefficients are calculated using a full model taking into account interactions with higher-order modes.

3.2 Initial analysis

Before analyzing the full geometry in detail, it is instructive to consider an initial evaluation of the Purcell factor and the efficiency on resonance as a function of the top mirror power reflection coefficient $R_{11}^t = \left|r_{11}^t\right|^2$ in order to get a feeling of the trade-off between the Purcell enhancement and the efficiency. In this initial analysis, we set $T_{11} = 1 - R_{11}^t$ and we choose $\Gamma_{HE11} = 0.88\Gamma_0$, $\Gamma_{Rad} = 0.04\Gamma_0$ and $\gamma_T = 0.92$ corresponding to realistic emission rates and taper transmission for an optimized nanowire geometry as discussed in more detail in Section 4 and in Appendices A and B. In this analysis we do not need to specify a value of the cavity length. The cavity length governs the linewidth as discussed in further detail in Section 5 as well as the spectral position of the resonance. However, in a Fabry-Perot cavity, the Q factor and the mode volume V are both linearly proportional to the cavity length, which when taking their

Optics EXPRESS

ratio in Eq. (6) then cancels out. The independence of F_P on the cavity length is also observed explicitly in Eq. (5).

We first consider an almost ideal bottom mirror reflection coefficient of $R_{11}^b = \left|r_{11}^b\right|^2 = 0.99$. The corresponding 1D Purcell factor $F_{P,Init}$ and efficiency ε_{Init} are shown in Fig. 2(a) as dashed curves.

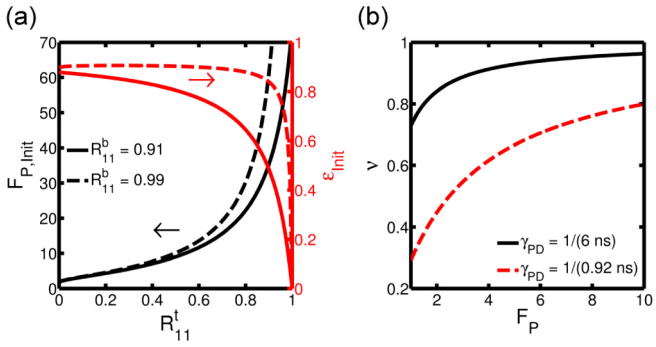

Fig. 2. (a) The 1D Purcell factor $F_{P,Init}$ (black) and the efficiency ε_{Init} (red) as function of bottom power reflection coefficient R_{11}^t. (b) The indistinguishability ν as function of F_P for γ_{PD} = 1/(6 ns) (black solid) and γ_{PD} = 1/(0.92 ns) (red dashed).

In the absence of DBR, the maximum efficiency is 0.897 and the Purcell factor is 1.8 due to the presence of the bottom mirror. As R_{11}^t increases towards unity, an $F_{P,Init}$ exceeding 20 is obtained for a slightly reduced efficiency of 0.892. While highly desirable, this combination of high Purcell enhancement and efficiency relies on the near-unity reflectivity of the bottom mirror, and at present a design for such a bottom mirror compatible with our small photonic nanowire radius has not yet been proposed. Of the various bottom mirror designs studied so far [40], the gold-silica mirror provides the best performance with a reflection coefficient R_{11}^b of 0.91. The Purcell factor and the efficiency for this value are given in Fig. 2(a) as full curves. A Purcell factor $F_{P,Init}$ larger than 20 can still be obtained, however this high $F_{P,Init}$ comes at the price of significant reduction of the efficiency due to transmission loss in the bottom mirror. A reasonable compromise appears for a reflection R_{11}^t of 0.35 where an $F_{P,Init}$ of 6.3 is obtained combined with a maximum theoretical ε_{Init} of 0.84. These numbers represent a relative improvement of more than 3 in the Purcell factor at a relative reduction in the efficiency of only 5%. We stress that the trade-off between high Purcell effect and high efficiency occurs due to the non-unity bottom mirror reflection.

The improvement in the indistinguishability of the emitted photons can be determined by considering a model for the indistinguishability ν in the Hong-Ou-Mandel experiment taking into account phonon-induced decoherence and spectral wandering. Assuming negligible timing-jitter (i.e. resonant excitation conditions), the indistinguishability of the emitted photons in the Purcell regime can be qualitatively captured by [11]

$$\nu = \frac{\Gamma_0 F_P + \Gamma_{Rad}}{\Gamma_0 F_P + \Gamma_{Rad} + 2\gamma_{PD}}, \tag{8}$$

where γ_{PD} is the dephasing rate, which in general will contain contributions from both phonon-induced processes and spectral diffusion. We note that while this simplistic model is expected to fully capture the effect of spectral diffusion and Purcell enhancement on the indistinguishability, coupling to phonons can be considerably more complicated, giving rise, for example, to phonon-modified emission rates which depend on the characteristics of the

Optics EXPRESS

QD in question, and which are not accounted for in the above expression [11,48]. These effects, however, are typically much weaker than the cavity-induced emission enhancement in which we are interested, and as such we adopt the simple model above which provides us with a qualitative understanding of how an increased Purcell factor can affect visibilities for generic QD samples. The implementation of the cavity introduces a phonon-induced dephasing of the zero-phonon line [11] absent in the bare taper geometry, and one effect which does require some consideration is the increased phonon-induced dephasing rate with an increased QD-cavity coupling strength [11,13]. Importantly, however, for a fixed QD-DBR distance h, the Purcell factor in our SPS design can be improved by increasing the Q factor, with the QD-cavity coupling strength (inversely proportional to the square-root of the mode volume) remaining approximately constant. As such we do not expect dephasing caused by either phonons or spectral diffusion to change appreciably as a function of the Purcell factor. In fact, in contrast to the dependence on the coupling strength, it was shown in Ref. [13] that an increase of the quality factor can lead to a monotonous increase of the indistinguishability. This mechanism is not captured by our model above, meaning that for our design, increases in indistinguishability with F_P may in fact be faster than suggested by Eq. (8), which should therefore be considered a conservative estimate of the behavior with F_P.

From Eq. (8) we can immediately see that since γ_{PD} does not depend on F_P, the indistinguishability will increase with the Purcell factor F_P attaining higher values for smaller values of the dephasing rate γ_{PD}. To give some experimentally feasible values, in Fig. 2(b) we plot the indistinguishability as a function of the Purcell factor for two fixed values of the total dephasing rate γ_{PD}. We use the bulk QD emission rate of $\Gamma_0 = 1/T_1 = 1/(1.16\text{ ns})$ experimentally determined for a photonic trumpet device in [49]. In this work the Stark effect was not used to stabilize the local charge environment, and the dephasing time $T_2 = 0.66$ ns was 3.5 times smaller than $2T_1$ leading to a dephasing rate of $\gamma_{PD} = 1/(0.92\text{ ns})$ represented in Fig. 2(b) by the red dashed curve. As expected, the Purcell effect enhances the indistinguishability, which is increased from 0.3 to 0.7 for cavity with an F_P of 6.3. We also consider a dephasing rate of $\gamma_{PD} = 1/(6\text{ ns})$ illustrated by the black curve. This value is representative of current experiments [23,24] for which dephasing processes are largely suppressed. For this parameter we see that values of 95% and above ought to be feasible. Finally, we note that these numbers are representative of photons having immediately exited the device, which could in principle be increased by introducing spectral filtering [21], though this would necessarily impair the efficiency of the source.

4. Element analysis

We now discuss the performance of the two sections. These studies will subsequently allow us to analyze the efficiency, the Purcell enhancement and the Q factor. The computations are performed using an eigenmode expansion technique [50] with improved perfectly matched layers [51]. The taper sections are modeled using a staircase approximation [52].

The first two logical tasks in the photonic nanowire SPS design are the determination of the nanowire radius R_0 at the position of the quantum dot allowing for efficient coupling to the fundamental HE_{11} mode and the determination of the opening angle and height of the bare taper geometry allowing for high transmission to the lens. These studies have been documented previously [32–35] and are presented in the Appendices A and B for completeness. Here, we simply summarize optimized parameters for the bare taper geometry in Table 2, and we refer the reader unfamiliar with the details of these calculations to the appendices.

Table 2. Bare taper geometry parameters.

R_0 (nm)	R_{top} (μm)	Opening angle α (°)	h_T (nm)	γ (0.4 NA)
114	2	10	21557	0.92

Optics EXPRESS

4.1 Section I: DBR in trumpet geometry

We now incorporate the DBR mirror into the bare structure with parameters of Table 2. The DBR is placed at a distance h from the QD as illustrated in Fig. 3(a). To optimize the reflection, the layer thicknesses should be ¼ optical wavelength. For a non-tapered DBR of fixed radius R such as that used in micropillar, the layer thickness t is trivially computed as $t = \lambda / (4\, n_{\text{eff}}(R))$, where $n_{\text{eff}}(R)$ is the effective index of the layer evaluated for the fixed radius R [53]. For a tapered DBR, however, the radius R and thus $n_{\text{eff}}(R)$ are varying along the nanowire axis. An opening angle of 10° leads to a modest effective index variation inside the layer, and we thus determine the layer thickness t from the effective index $n_{\text{eff}}(R_e)$ computed at the evaluation radius R_e at the center of the layer. Now, R_e is a function of t, which in turn depends on R_e. Starting from the 0-order thickness $t^{(0)} = \lambda / (4\, n_{\text{Bulk}})$, we use an iterative scheme to compute subsequent orders of the evaluation radius and the layer thickness until convergence is obtained as described in detail in the Appendix.

The number of DBR layer pairs represents an additional degree of freedom. To identify an optimum number of layer pairs, we study in Fig. 3(b) the power reflection as function of the QD-DBR distance h for a varying number of DBR layer pairs. We observe that the reflection improves slightly as h is increased. This is due to an improved overlap between the HE_{11} mode profiles in the GaAs/AlGaAs layer as the DBR layer radii increase with h. A large reflection above 0.7 is obtained for 10 DBR layer pairs. While this high reflection leads to strong Purcell enhancement, it also leads to strongly reduced efficiency due to an increased number of roundtrips in the cavity and bottom-mirror induced losses. However, we observe that a reflection of approximately 0.35 is obtained for 6 DBR layer pairs. According to the initial analysis in Section 3.2, 6 DBR layer pairs should result in a Purcell factor of about 7 at the minor price of a slightly reduced efficiency.

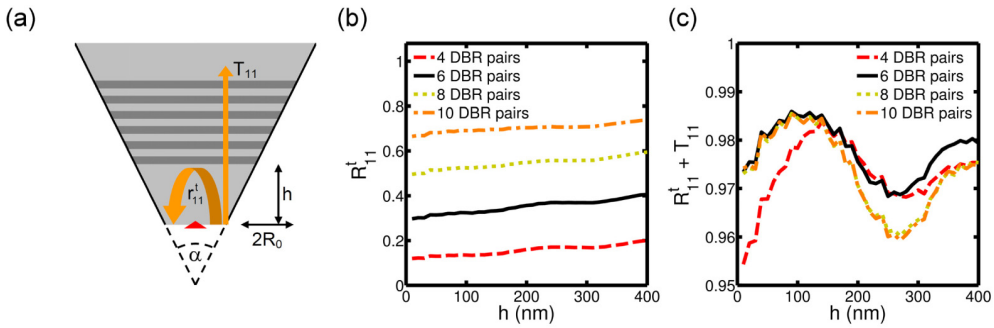

Fig. 3. (a) Illustration of the bottom part of the trumpet implementing a DBR. Reflection (b) and sum of reflection and transmission (c) as function of QD-DBR distance h for a varying number of DBR layer pairs.

Additionally, it is important that the DBR remains adiabatic, i.e., the sum of the power reflection R_{11}^t and transmission T_{11} of the fundamental mode should equal 1. This sum is plotted in Fig. 3(c) as function of h. We observe that the sum is generally above 0.95, indicating that the DBR indeed operates in an adiabatic regime.

4.2 Section II: Bottom metal mirror

Finally, we identify the geometrical parameters for the bottom metal mirror. The geometry is sketched in Fig. 4(a). The metal mirror generally provides a high broadband reflectivity. However, it is necessary to implement a silica spacer to avoid coupling to surface plasmons [40].

Having previously fixed $R_0 = 114$ nm and the opening angle $\alpha = 10°$, we first determine the ideal thickness of the silica layer h_g. The power reflection coefficient R_{11}^b is shown in Fig.

Optics EXPRESS

4(b) as function of R_0 for three values of h_g. We observe that a maximum reflection is obtained for a silica thickness h_g = 6 nm. We remark that this value used in the following is almost a factor of two smaller than the optimum thickness of ~11 nm identified in previous works [33,34,40], which was estimated for a cylindrical shape of the PW segment in contact with the bottom mirror.

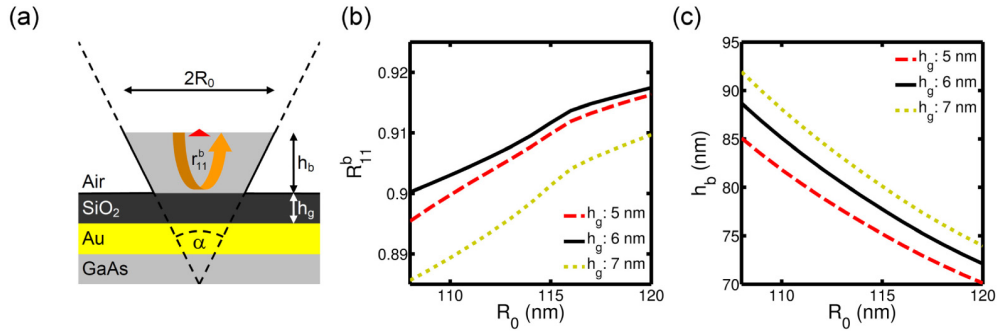

Fig. 4. (a) The bottom metal mirror geometry. Bottom metal mirror reflection (b) and optimum QD-mirror distance h_b (c) as function of R_0 for varying h_g. α = 10°.

Furthermore, we need to choose the optimum QD-mirror distance h_b. The QD should be placed at a field antinode to ensure a maximum coupling to the HE_{11} mode. The distance h_b corresponding to the antinode is shown in Fig. 4(c). For our choices of R_0, α, and h_g, the optimum distance ensuring that the quantum emitter is positioned at a field antinode is h_b = 79 nm. This number varies between 72 and 89 nm over the 14 nm range considered, indicating that the performance is somewhat sensitive to fabrication imperfections. The parameters for the bottom metal mirror are summarized in Table 3.

Table 3. Bottom metal mirror parameters.

R_0 (nm)	Opening angle α (°)	h_g (nm)	h_b (nm)	R_{11}^b
114 nm	10	6	79	0.91

5. Results for the full geometry

Having identified optimum geometrical parameters for the various elements, we now present the performance of the full photonic nanowire SPS implementing a DBR. The calculations are performed using the elements-splitting model presented in Section 3.1 with the geometrical parameters summarized in Tables 1-3.

5.1 Study for 6 DBR layer pairs

We initially fix the number of DBR layer pairs to 6 representing a good compromise between improved Purcell enhancement and high efficiency. Figure 5(a) presents the computed Purcell factor F_P as function of QD-DBR distance h and as function of wavelength λ. The introduction of the top DBR leads to the formation of a cavity and its resonance wavelengths thus depend on h. The resonances appear as slightly tilted lines with F_P reaching up to 7.4. Between the resonances the Purcell factor drops to values as low as 0.5. For our design wavelength λ of 925 nm, the resonances appear at approximately h = 10 nm, 200 nm, 380 nm and 550 nm. These values of h lead to similar Purcell enhancement, with slightly increasing F_P values for larger h due to improved reflection with h as discussed in Section 4.1.

Optics EXPRESS

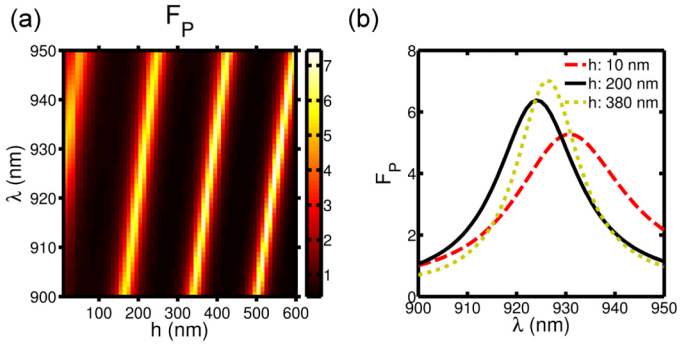

Fig. 5. (a) The Purcell factor F_P as function of QD-DBR distance h and wavelength λ. (b) The Purcell factor as function of λ for several values of h.

However, when choosing h we should also consider the linewidth to ensure that our design remains as broadband as possible. Since the Q factor increases with the cavity length, an increased h will lead to a reduced linewidth. The spectral behavior of the Purcell factor is shown in Fig. 5(b) for h = 10 nm, 200 nm and 380 nm. The h = 10 nm value shows the broadest resonance with a FWHM of 29 nm. However, this close proximity of the AlGaAs layer to the QD layer may significantly decrease the quantum efficiency of the QDs. For our final design, we thus chose the next resonance appearing at h = 200 nm, which features an F_P value of 6.4 and a FWHM of 20 nm.

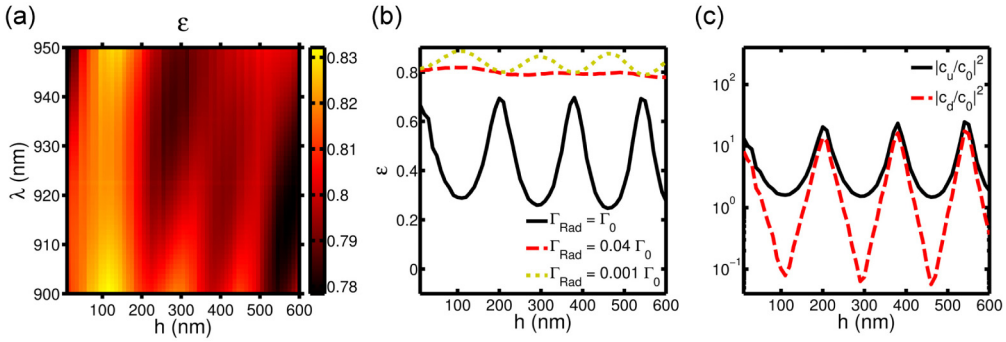

Fig. 6. (a) The total efficiency ε as function of QD-DBR distance h and wavelength λ for a 0.4 NA lens. (b) ε as function of h for several values of Γ_{Rad} for λ = 925 nm. (c) Normalized absolute squares of coefficients c_u and c_d as function of h.

The total efficiency ε for this design is shown in Fig. 6(a). While the efficiency does display weak variations discussed in the following, we observe the very interesting phenomenon that the high efficiency is maintained over the entire parameter range. This occurs in striking contrast to the microcavity pillar-based SPS, where high efficiency is only obtained at resonance. The origin of this broadband high efficiency is the suppression of spontaneous emission into radiation modes Γ_{Rad}, which is a characteristic feature of the photonic nanowire geometry, as discussed in Section 1. The Purcell factor may oscillate inside the parameter regime, however the mechanism ensuring efficient QD-HE_{11} mode coupling is the dielectric screening effect, not high enhancement, and high efficiency is thus maintained even for low F_P. To verify this interpretation, we set Γ_{Rad} equal to the rate Γ_0 for a bulk medium by hand and examine the resulting efficiency for λ = 925 nm depicted as the black full curve in Fig. 6(b). We observe that the efficiency now depends strongly on F_P with maxima occurring exactly at the resonances illustrated in Fig. 5(a).

It is also of interest to understand the opposite limit with strongly suppressed background emission rate and we now set $\Gamma_{Rad} = 10^{-3}\ \Gamma_0$. Remarkably, the corresponding dotted yellow

Optics EXPRESS

curve in Fig. 6(b) displays the opposite behavior as compared to the previous case with maximum efficiencies at the QD-DBR heights h corresponding to minima of the Purcell factor. This surprising tendency can be understood from an analysis of the variations of the c_u and c_d coefficients defined in Eqs. (2)-(3) and displayed in Fig. 6(c). For QD-DBR heights h corresponding to a resonance, the reflection coefficients r_{11}^t and r_{11}^b both add up constructively with unity and the c_u and c_d coefficients take similar values. Since the bottom mirror geometry remains unchanged when h is varied, the phase of r_{11}^b doesn't change and r_{11}^b always adds up constructively with unity. However, the phase of r_{11}^t strongly depends on the QD-DBR distance h and off resonance r_{11}^t adds up destructively with unity, leading to a significant relative suppression of the absolute square of the c_d coefficient as compared to c_u as observed in Fig. 6(c). Inspection of Eq. (4) then reveals that for strongly suppressed c_d and Γ_{Rad} coefficients, the total spontaneous emission rate will be dominated by its contribution in the forward direction.

The efficiency for the actual background rate $\Gamma_{Rad} = 0.04\ \Gamma_0$ is displayed as the dashed red curve in Fig. 6(b). We observe that for this realistic Γ_{Rad} value, we are at the boundary between the two regimes discussed previously with neither strong enhancement nor suppression of the efficiency at the resonances. This broadband high efficiency for a cavity QED system is a unique feature of the photonic nanowire SPS design approach. It allows for high efficiency even if the quantum emitter is not exactly on resonance and thus provides good tolerance towards spectral misalignment.

Table 4. Microcavity mode volumes.

	Photonic trumpet (h = 200 nm)	Micropillar [23]	Photonic crystal L3 [54]	Photonic crystal H0 [55]
$V\ (\lambda/n)^3$	0.71	30	0.77	0.23

While our model for the Purcell factor Eq. (5) does not require the explicit calculation of the cavity mode volume V, it is instructive to compare its value for the photonic trumpet cavity to other state-of-the-art microcavity systems. The mode volume can be estimated from Eq. (6) from our knowledge of F_P and Q. The resulting value is shown in Table 4 together with typical values for state-of-the-art microcavity systems. As expected, the mode volume of our design of 0.71 $(\lambda/n)^3$ is almost two orders of magnitude smaller than that of a typical micropillar geometry. Additionally, it is comparable to values otherwise obtained only in planar structures, for which highly efficient outcoupling of light remains a challenge.

5.2 Study of variations of number of DBR pairs

In this section, we study the influence of the number of DBR layer pairs on the performance.

When increasing the number of DBR layer pairs, the Purcell factor is improved at the resonance wavelengths as shown in Fig. 7(a). The corresponding efficiency is shown in Fig. 7(b), and we observe that the improved Purcell enhancement comes at the cost of significantly reduced efficiency, as also discussed in Section 3.2. The Purcell factor as function of wavelength is depicted in Fig. 7(c), and we observe that the increase in reflectivity also influences the FWHM, which is reduced to 4 nm for 14 DBR layer pairs.

Optics EXPRESS

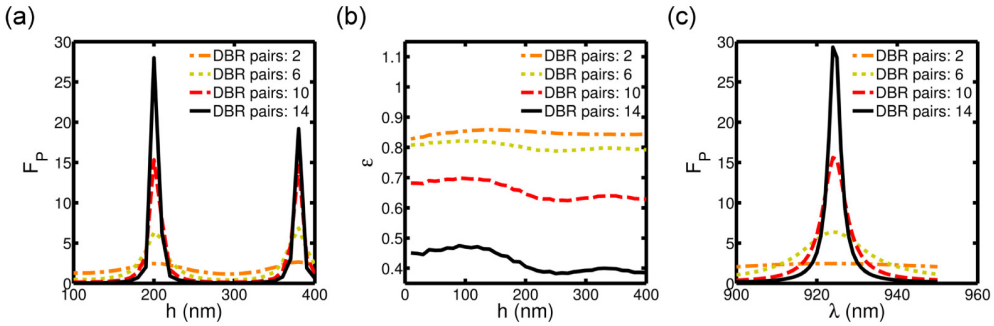

Fig. 7. F_P (a) and ε (b) as function of QD-DBR distance h for several numbers of DBR layer pairs for $\lambda = 925$ nm. (c) F_P as function of λ for $h = 200$ nm. A 0.4 NA lens is considered.

5.3 Tolerance study for spatial QD misalignment

Due to the length of the top taper, deterministic positioning using an in situ method is not immediate and the original demonstration [15] of the photonic trumpet SPS featured randomly positioned QDs. It is thus of relevance to understand the influence of spatial misalignment of the emitter in the lateral plane. In cylindrical coordinates, the dipole moment of a QD can be oriented either along the **r** or the **ϕ** unit vectors as illustrated in Fig. 8(a), and for an off-axis emitter, the spontaneous emission rates into the HE_{11} mode and into radiation modes are different for the two in-plane orientations. The rates Γ^r_{HE11} and Γ^ϕ_{HE11} for an infinite nanowire are shown in Fig. 8(b) as function of emitter-axis distance ρ together with the rates Γ^r_{Rad} and Γ^ϕ_{Rad} all normalized to the rate Γ_0 in a bulk medium. While the rates into the fundamental mode display similar behavior, the orientation has significant influence on the spontaneous emission rate into radiation modes. For the r orientation, this emission is suppressed in most of the nanowire, whereas it increases rapidly for increasing ρ for the ϕ orientation. The coupling to the fundamental waveguide mode is usually quantified using the spontaneous emission β factor defined as $\beta = \Gamma_{HE11} / \Gamma^{NW}_T$, where $\Gamma^{NW}_T = \Gamma_{HE11} + \Gamma_{Rad}$ is the total emission rate for the infinite nanowire. The corresponding β factors are presented in Fig. 8(c). We observe that, while β^r remains high, β^ϕ drops quickly for increasing ρ. Additionally, we may consider an emitter with isotropic in-plane emission. The corresponding β^i can be computed using $\Gamma^i_{HE11} = (\Gamma^r_{HE11} + \Gamma^\phi_{HE11})/2$ and $\Gamma^i_{Rad} = (\Gamma^r_{Rad} + \Gamma^\phi_{Rad})/2$, and we observe that β^i remains above 0.59 when the emitter is closer to the axis than to the nanowire boundary.

Optics EXPRESS

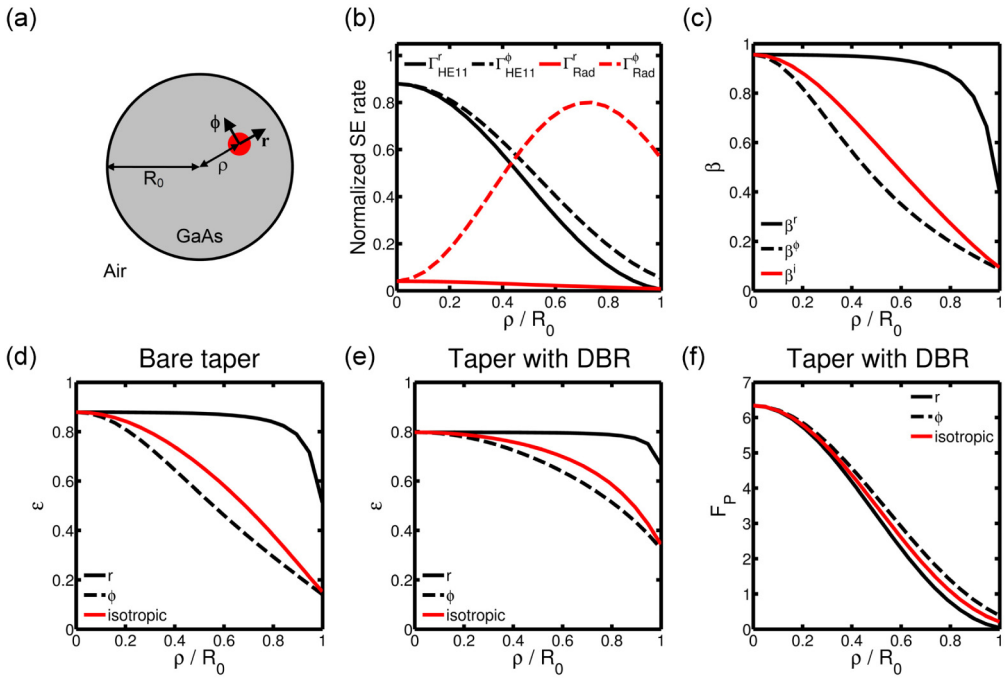

Fig. 8. (a) Lateral nanowire geometry with an off-axis QD. (b) Normalized spontaneous emission rates as function of emitter-axis distance ρ for dipole moments aligned along $\mathbf{r}$ and $\boldsymbol{\phi}$. (c) Associated β factors for the infinite nanowire. The efficiency ε of a photonic nanowire SPS featuring (d) a bare taper and (e) a taper implementing a DBR. (f) Associated Purcell factor. λ = 925 nm and R_0 = 114 nm.

The efficiency for the full photonic trumpet geometry in the absence of DBR mirror is plotted in Fig. 8(d). The absence of the DBR leads to a maximum efficiency of 0.89 for an on-axis emitter. As the emitter is displaced from the axis, the efficiencies largely reproduce the behavior observed for the β factors in Fig. 8(d), and we observe that the efficiency is above 0.66 for an isotropic emitter closer to the center than the boundary. We now study the efficiency presented in Fig. 8(e) for a taper implementing a DBR with 6 layer pairs. While the general behavior consisting of a reduced efficiency for the ϕ orientation is reproduced, this geometry benefits from the Purcell enhancement of the spontaneous emission into the cavity mode leading to an improved tolerance towards spatial misalignment. Indeed, we observe that the efficiency is above 0.73 for an isotropic emitter closer to the center than the boundary and the efficiency is now larger than 0.32 even for a QD at the very boundary. For photonic trumpets with randomly positioned QDs, we reach the surprising conclusion that the implementation of a DBR may actually improve the efficiency as compared to the bare case.

Finally, the influence of misalignment on the Purcell factor is presented in Fig. 8(f). Since F_P is proportional to Γ_{HE11} which in turn is proportional to the electric field strength of the HE_{11} mode along the orientation of the dipole, the Purcell factor simply reflects the Gaussian-shaped lateral field profile of the fundamental mode. For the isotropic dipole, we observe that the Purcell factor remains above 3.5 for an emitter closer to the axis than the boundary.

5.4 Tolerance study of the taper opening angle α

The growth recipe presented in the Appendix is optimized for an opening angle of $\alpha = 10°$. In this section, we investigate the performance of a design based on the growth recipe, where the opening angle α is varied to understand the tolerance towards fabrication imperfections. In this study we assume that R_0 = 114 nm and h_T = 21557 nm. Variations in α thus lead to variations in the top radius R_{top}.

Optics EXPRESS

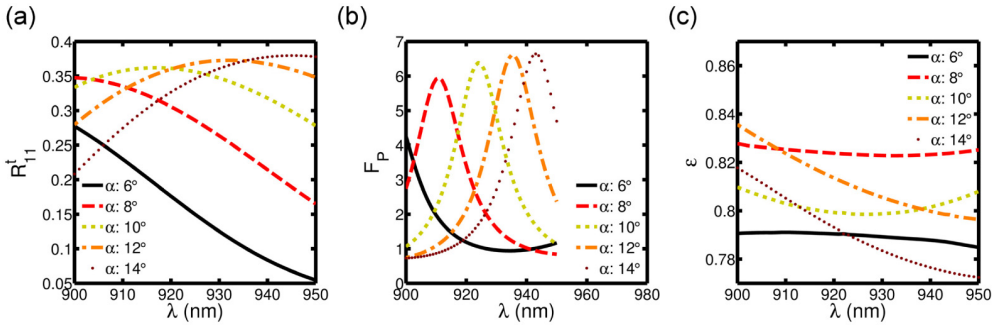

Fig. 9. The top reflection coefficient (a), F_P (b) and ε (c) as function of λ for varying opening angle α. h = 200 nm and a 0.4 NA lens is considered.

The DBR reflection coefficient R^t_{11} is plotted in Fig. 9(a) as function of wavelength. The maximum reflection increases slightly with α due to improved DBR performance for the resulting larger DBR layer diameters as discussed in Section 4.1. The position of maximum reflection redshifts for increasing tapering angles. The consequence for the resonance wavelength is shown in Fig. 9(b), and we observe that the effect of an increase (decrease) in the opening angle on the Purcell factor is a red (blue) shift of the resonance. Additionally, the Purcell factor is slightly improved for larger angles due to the improvement in R^t_{11}. The efficiency is depicted in Fig. 9(c), which shows that the influence of variations of the opening angle on ε is only a few percent within the regime studied.

6. Discussion

The design proposed in this paper features a Purcell factor on resonance of 6.4 with a remarkable 20 nm linewidth enabled by the ultrasmall mode volume V of 0.71 $(\lambda/n)^3$. Let us now discuss how the performance could be further improved.

The mode volume V of the design is governed mainly by the choice of R_0 and h. The nanowire radius R_0 cannot be reduced significantly as the nanowire quickly becomes too thin to support a well-confined mode. Also, h has already been chosen as small as possible to reduce the cavity length. The Purcell factor can be increased by improving the Q factor of the cavity, e.g. using a large number of DBR layer pairs. However, the broadband nature of photonic nanowire approach represents a key asset enabling broadband tuning and entangled photon pair generation. An increase in Q will reduce the linewidth of our design and thus requires careful consideration.

The efficiency of our design is reduced by 6% compared to the bare trumpet taper without DBR. Increasing the Purcell enhancement by increasing the DBR reflectivity leads to significantly reduced efficiency. However, this trade-off can be overcome by increasing the bottom mirror reflection coefficient. The metal-silica bottom mirror with a fairly high reflection of 0.9 and fairly simple flip-chip fabrication has represented an attractive bottom mirror strategy for the photonic nanowire SPS. However, in the pursuit of near-unity efficiency, a higher bottom mirror reflection will be needed. Such a bottom mirror can be realized as, e.g., another inverted DBR taper section leading to a photonic nanowire with hour-glass shape, and the development of a new fabrication technique allowing the production of such geometry would thus be desirable.

The proposed photonic nanowire design implements a weak cavity QED effect, and a comparison with the microcavity pillar SPS design is natural. A major difference between the two is the spectral alignment. In the photonic nanowire SPS, the efficiency is insensitive to the alignment. The full Purcell enhancement is still only obtained on resonance, however the 20 nm linewidth results in a reasonable chance of spectral overlap with a QD. Additionally, this linewidth should be sufficient to observe entangled photon emission from the exciton-

Optics EXPRESS

biexciton cascade. Furthermore, the broad linewidth paves the way for tunable single indistinguishable photon emission enabling e.g. frequency locking to a well-known atomic transition [56,57]. This tuning can be realized by implementing metal contacts [34] and using the Stark effect, or by applying mechanical stress on the QD, which allows for a large tuning range [58]. On the other hand, for a micropillar SPS with a typical Q factor of the order of a few thousand, an in situ fabrication technique allowing for spectral alignment [22] is in practice a requirement to achieve high efficiency, Purcell enhancement and indistinguishability. Additionally, the tunability is limited by the narrow linewidth.

While our design does not require an in situ fabrication technique, the possibility of controlling spectral and spatial alignment is clearly attractive. However, with typical taper heights of 10-30 μm, the identification of QDs with current in situ techniques appears unfeasible. Also, whereas the coupling of the micropillar cavity mode to the lens can be made arbitrarily close to unity using a highly asymmetric pillar design, the efficiency of the photonic nanowire SPS is limited by the metal mirror reflection coefficient of 0.9. The implementations of spectral and spatial alignment as well as a significantly higher bottom mirror reflection strategy thus represent open challenges for future photonic nanowire SPS development.

7. Conclusion

This article presents a complete photonic nanowire SPS design based on the inverted trumpet taper and implementing a weak cavity effect. The cavity is realized by implementing a DBR in the trumpet allowing for Purcell-enhanced spontaneous emission, which acts to reduce the impact of decoherence sources on photon indistinguishability.

We have proposed a simple model based on an elements-splitting approach to describe the Purcell enhancement, the Q factor and the total SPS efficiency. All the elements of the design were analyzed in detail for a GaAs-based SPS. A bare trumpet was initially studied and geometrical parameters were identified allowing for a transmission of 0.92 to the Gaussian profile of a 0.4 NA lens. Subsequently, the DBR was incorporated. The resulting Purcell enhancement was analyzed as function of DBR position and wavelength. Furthermore, the influence of the number of DBR layer pairs and the taper opening angle was studied.

It was shown that the use of 6 DBR layer pairs represents a good compromise between high Purcell enhancement and efficiency. Indeed, a Purcell factor of 6.4 is achieved combined with a FWHM linewidth of 20 nm and a maximum total SPS efficiency of 0.8. Larger Purcell factors are easily obtained by increasing the number of DBR layer pairs, at the cost of decreased efficiency and operation bandwidth.

Finally, we have compared our design to the micropillar SPS design approach, and we have outlined future open challenges within photonic nanowire SPS engineering.

Acknowledgements

This work was funded by project SIQUTE (contract EXL02) of the European Metrology Research Programme (EMRP). The EMRP is jointly funded by the EMRP participating countries within EURAMET and the European Union. NG acknowledges additional support from the Danish National Research Council for Technology and Production (LOQIT Sapere Aude grant DFF # 4005-00370).

Appendix A: QD in GaAs nanowire

In this section we identify the nanowire radius at the position of the QD for maximum coupling to the fundamental HE_{11} mode. Let us consider the infinite nanowire geometry illustrated in Fig. 10(a) with a QD with in-plane dipole moment placed in the center. The total spontaneous emission rate Γ_T^{NW} for the infinite nanowire geometry as well as the rates Γ_{HE11} into the fundamental mode and Γ_{Rad} into radiation modes are shown in Fig. 10(b) as function of nanowire radius R_0. The rates are normalized to the value Γ_0 in a bulk GaAs material.

Optics EXPRESS

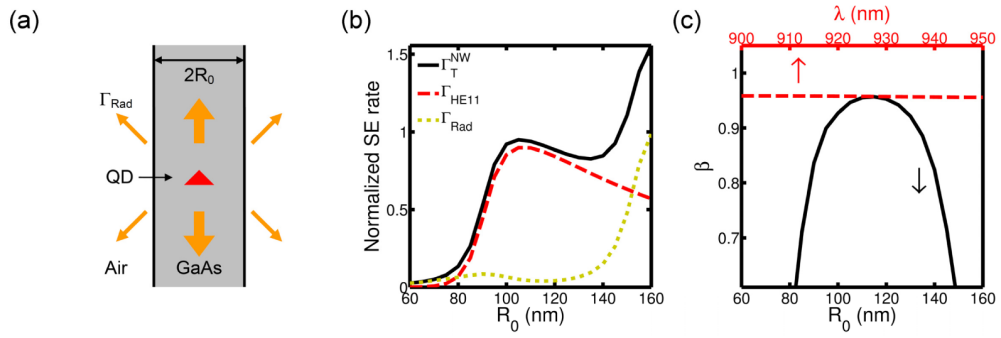

Fig. 10. (a) Infinite nanowire geometry. (b) Normalized spontaneous emission rates as function of nanowire radius R_0. (c) Spontaneous emission β factor as function of R_0 for λ = 925 nm (black full curve) and as function of λ for R_0 = 114 nm (red dashed curve).

For short radii, the spontaneous emission is suppressed due to a geometrical field-screening effect [31]. However, for larger radii almost all of the emitted light is coupled to the HE_{11} mode. This preferential coupling is quantified using the spontaneous emission β factor defined as $\beta = \Gamma_{HE11} / \Gamma_T^{NW}$ and plotted in Fig. 10(c) as function of R_0 and wavelength λ. Inspection of the full black curve reveals a β above 0.9 over a 40 nm range indicating good tolerance towards fabrication imperfection. Furthermore, a maximum β of 0.96 is obtained for R_0 = 114 nm, where $\Gamma_{HE11} = 0.04\Gamma_0$ and the spontaneous emission into radiation modes is as low as $\Gamma_{Rad} = 0.04\Gamma_0$. The wavelength dependence for this value of R_0 is given by the red dashed curve. It is almost flat over the 50 nm wavelength range, and this efficient broadband coupling is a key asset of the photonic nanowire design approach.

Appendix B: Bare trumpet geometry

In this section, we identify geometrical parameters ensuring high transmission to the lens for the bare taper geometry in the absence of a DBR. The geometry is illustrated in Fig. 11(a). The ideal refractive index n_{AR} of the anti-reflection (AR) coating is n_{AR} = sqrt(n_{GaAs}) = 1.87. We choose silicon nitride as AR material with an index of 1.99 sufficiently close to the ideal value to provide a transmission of 0.996. The thickness h_{AR} of the anti-reflection coating is chosen as $\lambda/(4n_{Si3N4})$ and R_0 is fixed at 114 nm as discussed earlier.

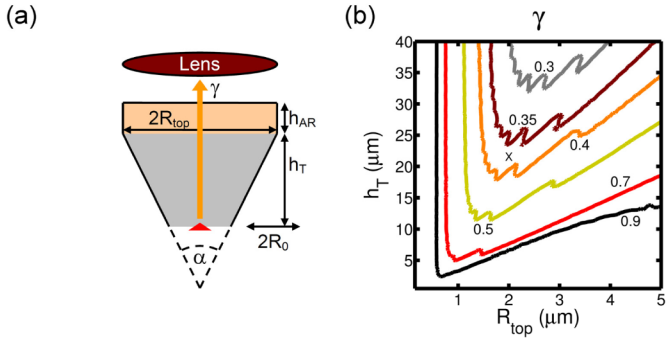

Fig. 11. (a) Illustration of the bare trumpet in absence of DBR. (b) Contour plot with lines defining transmission γ above 0.9 for the numerical apertures listed in the figure. The cross marks the chosen bare parameters in Table 2. Reprinted from Ref .[35] with the permission of AIP Publishing.

Let us now study the transmission γ to the lens as function of the total taper height h_T and the top nanowire radius R_{top} to determine an optimum parameter set. The calculation of γ includes an overlap integral with a Gaussian function, and γ thus represents the transmission

Optics EXPRESS

to a Gaussian mode profile. The computed transmission is given in Fig. 11(b). The contour lines define the parameters for which the transmission is equal to 0.9 for a lens with given numerical aperture (NA). For small values of R_{top} and h_T, a large NA lens is required. For a fixed R_{top}, an increasing taper height h_T leads to an improved adiabatic transition of the HE_{11} mode [35] and the transmission to the lens is improved. For a fixed value of h_T, an extension of the top radius R_{top} initially leads to improved transmission, until the point where the adiabatic transition breaks down. Generally, for high transmission a large taper height is preferred [35].

For our design, we choose a realistic opening angle of 10° comparable to that of previously fabricated photonic trumpets [15,35] and a top nanowire radius R_{top} of 2 μm. These geometrical parameters, summarized in Table 2, represent a good compromise allowing for high transmission γ of 0.92 while keeping a reasonable size of the structure.

Appendix C: Growth recipe

Here we present the growth recipe for the geometry with parameters listed in Tables 1-3 for a QD-DBR distance h of 200 nm. The thicknesses of the DBR layers should be chosen to ensure that each layer is ¼ optical wavelength. However, the effective index of the fundamental mode varies with position inside each layer.

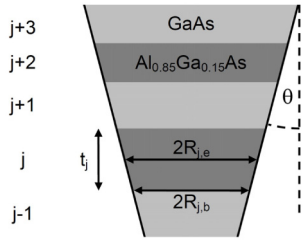

Fig. 12. The DBR mirror geometry.

Refering to Fig. 12, the thickness t_j of the DBR layer j is computed from

$$t_j \equiv t_j^{(1)} \equiv \frac{\lambda}{4n_{\text{eff}}(R_{j,e}^{(1)})}, \tag{9}$$

where $n_{\text{eff}}(R_{j,e}^{(1)})$ represents the effective index of the HE_{11} mode computed at the evaluation radius $R_{j,e}^{(1)}$. This radius is determined as

$$R_{j,e}^{(1)} = R_{j,b} + \frac{\tan\theta}{2} t_j^{(0)}. \tag{10}$$

Here $R_{j,b}$ refers to the radius at the bottom of the layer j, the side-wall angle θ equals $\alpha/2$ and $t_j^{(0)} = \lambda/(4n_j)$ is the ideal thickness of a 1D DBR layer.

This procedure represents the first iteration of a loop where $(R_{j,e}^{(1)}, t_j^{(1)})$, $(R_{j,e}^{(2)}, t_j^{(2)})$, $(R_{j,e}^{(3)}, t_j^{(3)})$ etc. are evaluated until convergence is obtained. However, $t_j^{(1)}$ and $t_j^{(2)}$ differ by less than a nm and thus the thickness $t_j^{(1)}$ from the first order is retained.

Optics EXPRESS

Table 5. Growth recipe

Layer #	Material	Thickness t_n (Å)	Comment
1	GaAs	790	QD-Metal mirror distance
2	InAs	0	QD layer
3	GaAs	2000	h = 200 nm
4	$Al_{0.85}Ga_{0.15}As$	1182	1st DBR pair
5	GaAs	854	
6	$Al_{0.85}Ga_{0.15}As$	1052	2nd DBR pair
7	GaAs	809	
8	$Al_{0.85}Ga_{0.15}As$	986	3rd DBR pair
9	GaAs	779	
10	$Al_{0.85}Ga_{0.15}As$	944	4th DBR pair
11	GaAs	759	
12	$Al_{0.85}Ga_{0.15}As$	915	5th DBR pair
13	GaAs	745	
14	$Al_{0.85}Ga_{0.15}As$	893	6th DBR pair
15	GaAs	734	
16	$Al_{0.85}Ga_{0.15}As$	877	7th DBR pair
17	GaAs	725	
18	$Al_{0.85}Ga_{0.15}As$	864	8th DBR pair
19	GaAs	718	
20	$Al_{0.85}Ga_{0.15}As$	854	9th DBR pair
21	GaAs	712	
22	$Al_{0.85}Ga_{0.15}As$	845	10th DBR pair
23	GaAs	707	
24	$Al_{0.85}Ga_{0.15}As$	838	11th DBR pair
25	GaAs	704	
26	$Al_{0.85}Ga_{0.15}As$	832	12th DBR pair
27	GaAs	700	
28	$Al_{0.85}Ga_{0.15}As$	827	13th DBR pair
29	GaAs	697	
30	$Al_{0.85}Ga_{0.15}As$	823	14th DBR pair
31	GaAs	h_{Final}	
32	Si_3N_4	1162	AR coating

This growth recipe (Table 5) includes thickness information for up to 14 DBR layer pairs. A reduced number of layer pairs can be implemented simply by skipping the last pairs.

The final GaAs layer thickness h_{Final} is given by

$$h_{Final} = h_T - \sum_{j=3}^{j=j_{max}} t_j. \tag{11}$$

where j_{max} is the last AlGaAs layer included.

In the case of 6 DBR layers pairs, the DBR pairs from 7 to 14 would be skipped and j_{max} = 14. For the geometrical parameters of Table 2, a h_{Final} of 203655 Å is obtained.